Technology Explanation

Prototype of Electric Mechanical Actuator for Replacing Hydraulic Equipment

SATO Kosuke, SHIBAHARA Daichi, HAKAMADA Shinichiro

Abstract

A prototype of an electric mechanical actuator with a cylindrical linear motor was verified, and the actuator is for replacing hydraulic equipment and the motor is jam free.

In order to increase the force density of the actuator, an airgap area was expanded by layout of the outer stator (magnet) and inner armature, and the Halbach arrangement on the stator and trapezoid teeth on the armature were applied to the motor. And in order to eliminate any inner force between the stator and armature, a movable armature was placed in a sleeve with wear rings.

A verification test showed that the maximum force was 4,741N@240mm/s, the mass was 9.49kg and the force density of the actuator was 499.6N/kg. We expect that the electric mechanical actuator can replace hydraulic equipment.

1 Introduction

Electrification of aircraft equipment has been promoted to improve the fuel efficiency and serviceability [1]. Because of jamming of the electric mechanical actuators attributable to the ball screws, however, the critical equipment including the flight control system still use hydraulic actuators [2]. The authors have then focused on the cylindrical linear motor that can be characterized by its jam free feature. However, this motor involves a problem that the force density is lower than that of hydraulic equipment (commercially available electric actuator: 56 to 133 N/kg, hydraulic equipment: 6,000 N/kg [3]).

Previous prototyping (Table 1) showed a force density of 109 N/kg for the primary prototype or 292.8 N/kg [4] for the secondary prototype, both of which are still below the target level of 600 N/kg [5] for the electric mechanical actuator to be able to replace the hydraulic equipment.

This paper discusses problems with the secondary prototype to set up improvement measures and then derive a structure of a tertiary prototype along with its calculation model with a target force density of 600 N/kg. The paper also provides the results of a verification test.

Table 1 Previous prototyping

	Force density	Improvements
Commercially available product	56N/kg	(Benchmark)
Primary prototype	109N/kg	Higher drive current (5.6 A → 11.2 A)
Secondary prototype	292.8N/kg	Multipolar (8p24s → 16p24s) Coreless → Core type Lighter structure (4.3 kg → 1.5 kg)

2 What is the Cylindrical Linear Motor?

The operating principle of the cylindrical linear motor is shown in Fig. 1. The motor consists of a shaft that serves as a field magnet and a case that serves as an armature. The shaft is installed inside the case in such a manner that can be axially operated. Thus, the motor has a very simple basic structure.

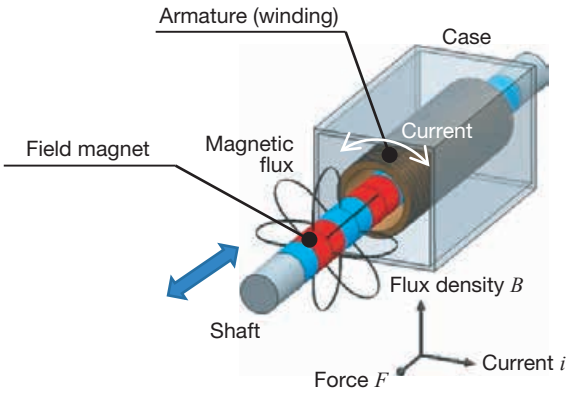

Fig. 1 Operating principle of cylindrical linear motor

The magnetic flux (flux density B) occurs in the radial direction of the shaft and the current i flows along the winding inside the case. When the magnetic flux interlinks with the current, a force F occurs in the axial direction of the shaft according to the Fleming's left-hand rule for electric motors. The direction of the force F can be changed by phase control of the current i.

The force F can be expressed by Equation (1) (where B is the flux density, L the winding length and i the current):

$$F = BiL \quad (1)$$

The force density cannot always be increased just by increasing the winding length L since this will also increase the mass. The current i has been already set to the upper limit current density in the primary and secondary prototypes. Therefore, to increase the force density, the flux density B must be increased. In other words, the number of lines of magnetic flux that interlink with the current needs to be increased by modifying the magnetic circuit of the motor. The core structure employed in the secondary prototype shown in Fig. 2 is an example of modifications with a substantially improved magnetic flux density B.

3 Structure of Tertiary Prototype

3.1 Problems with Secondary Prototype

The problems with the secondary prototype can be summarized as follows. As in Fig. 1, the movable magnet is located inside the stationary armature with an airgap between them so that they can slide with each other. This structure involves two problems:

- Insufficient force density
- Occurrence of an inner force between the magnet and armature

As described in section 1, the electric mechanical actuator has an insufficient force density to replace the hydraulic equipment.

The inner force between the magnet and armature is well balanced if the magnet is perfectly aligned. In reality, however, the magnet may be slightly eccentric due to its own deflection. According to the results of a calculation of the eccentricity and inner force shown in Fig. 3, the inner force is approx. 1,200 N on an assumption that the allowable magnet eccentricity is 0.5 mm. For the secondary prototype, a polycarbonate pipe was inserted between the magnet and armature as a provisional measure to structurally control the allowable eccentricity to 0.1 mm.

3.2 Improvement of Motor Structure

An improved motor structure for the tertiary prototype is shown in Fig. 4. The specifications of the secondary and tertiary prototypes are listed in Table 2. All figures shown in Table 2 indicate design values except mass which indicates actual measurements. Because of the limitations by the internal potentiometer, the tertiary prototype has a stroke of 90 mm in spite of the mechanical stroke of 162 mm, and similarly has a total length of 731.84 mm in spite of the mechanical total length of 641.84 mm.

The tertiary prototype is different in structure from the secondary prototype mainly in two points:

- Arrangement with the outer stator/magnet and the inner armature
- A sleeve inserted between the stator/magnet and armature

Improvement measures related to these structural differences include to expand the airgap area to make up for the insufficient force density, the Halbach arrangement of the stator/magnet, the trapezoid teeth of the armature, and the sleeve structure to decrease the inner force between the armature and stator/magnet.

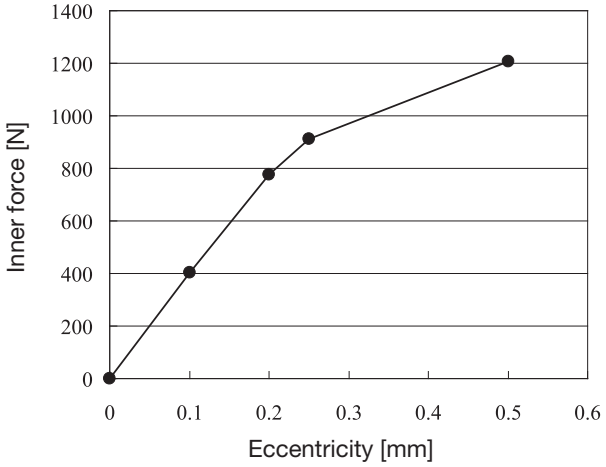

Fig. 3 Inner force between magnet and armature (analysis)

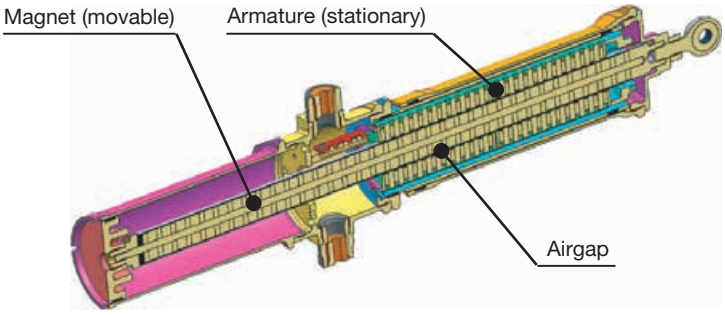

Fig. 2 Structure of secondary prototype

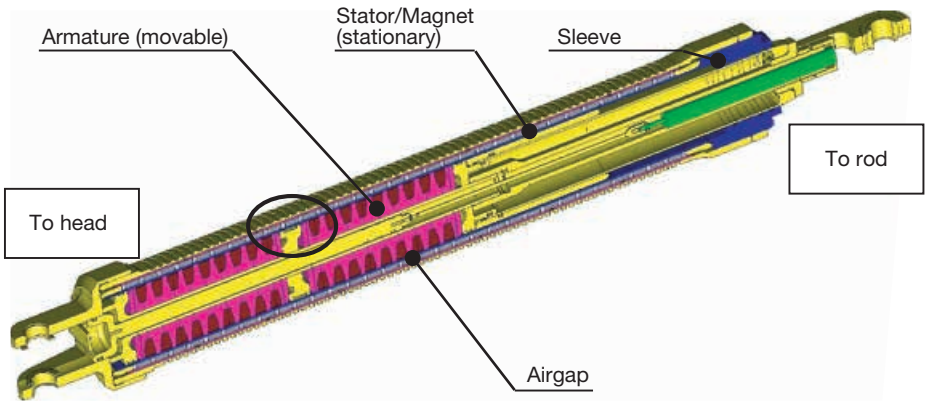

(a) Overview

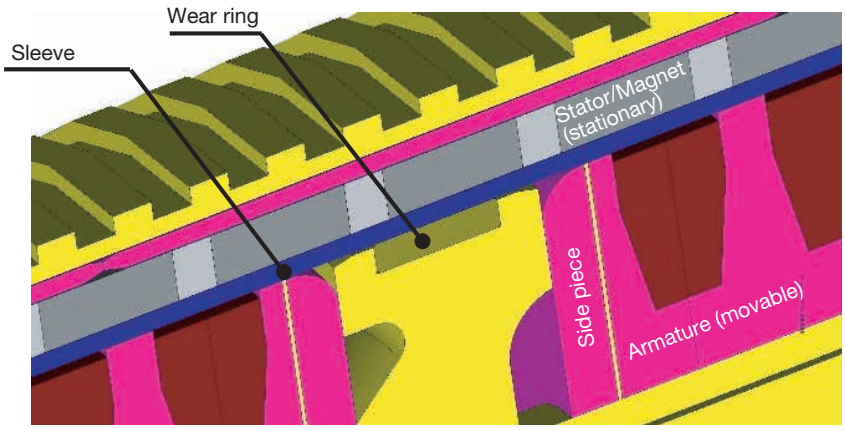

(b) Enlarged view of elliptical part

Fig. 4 Structure of tertiary prototype

Table 2 Specifications

	Tertiary prototype	Secondary prototype
Actuator		
Mount	Rod end	Trunnion
Total length - Outer dia.	731.84(641.84)mm - ø89mm	555.7mm-ø90mm
Stroke	90(162)mm	162.2mm
Mass	9.49kg	6.9kg
Motor		
Structure	16p18s, core type	16p24s, core type
Arrangement (In-Out)	Armature-Magnet	Magnet-Armature
Power supply	DC 270V	DC 707V
Allowable magnet temperature	150°C	90°C
Cooling	Natural air cooling	Natural air cooling
Stroke sensor	Potentiometer	Hall device

3.2.1 Larger Airgap Area

Increasing the airgap area will enlarge the magnet surface area, resulting in more lines of magnetic flux generated by the magnet. Naturally, the flux density B in Equation (1) is higher. With the stator/magnet located outside, the tertiary prototype has an airgap area of ø61 mm x 247.94 mm, which is larger than that of the secondary prototype (ø24 mm x 208.98 mm). The airgap area of the tertiary prototype is 3.01 times larger than that of the secondary prototype.

However, the inner-armature arrangement with the actuator's outer diameter almost equivalent to that of the secondary prototype (Table 2) makes the outer diameter of the armature core smaller, which causes the armature core to be more likely to have magnetic saturation. Countermeasures to this problem are the trapezoid teeth described in 3.2.3 and the phase lead compensator for current control stated in 4.1.

3.2.2 Halbach Arrangement

The motor magnets can be arranged in different ways depending on the direction of magnetization: Halbach and counter arrangements. The tertiary prototype uses the Halbach arrangement. Fig. 5(a) shows the flow of magnetic flux for the Halbach arrangement and Fig. 5(b) for the counter arrangement. Triangles appearing in the figures show the direction of magnetization of the magnet.

Since the Halbach arrangement of magnets generates deflected magnetic flux, installing an armature on the deflected side of the magnetic flux will obtain more flux linkage with a same magnet volume. Furthermore, different magnet materials are used for the radial and axial

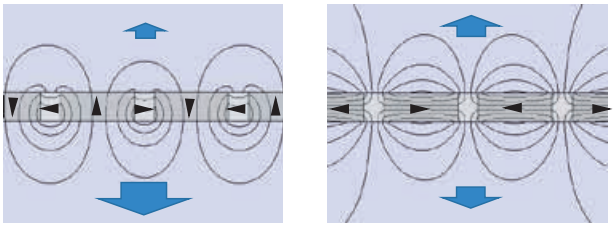

(a) Halbach arrangement (b) Counter arrangement

Fig. 5 Magnetic flux from magnets

magnetizations to achieve the allowable magnet temperature of 150˚C while keeping the force at a certain level (Patent public No. 2019-122072).

3.2.3 Trapezoid Teeth

Fig. 6 shows the distribution of flux density of trapezoid teeth used in the tertiary prototype and that of rectangular teeth as a comparison target. Magnetic saturation is colored in red. Note that both the windings for trapezoid and rectangular teeth have a same cross-sectional area.

For the rectangular teeth, the magnetic flux is concentrated in the root, causing a bottleneck of the flux. For the trapezoid teeth with an almost uniform area of the radial magnetic path, the magnetic flux is distributed in the whole teeth to realize a smooth flow of magnetic flux. The trapezoid teeth has an advantage of a higher flux density B (WO2019/102761A1, Patent public No. 2019-097377).

3.2.4 Sleeve Structure

As shown in Fig. 4, the armature is installed together with wear rings inside the aluminium alloy sleeve so that the armature can slide in the axial direction via the rings. The inner surface of the sleeve is coated with a hard anodic oxide to ensure the sliding property. The wear rings is made of aircraft fluoroplastic.

The sleeve structure prevents the armature from becoming eccentric and the inner force between the stator/magnet and armature is balanced in the radial direction, resulting in almost zero (Patent public No. WO2019/202758A1).

3.3 Motor Assembly

The motor assembly is shown in Photo 1.

Photo 1(a) shows the motor being assembled in which 56 magnets, among the total 63, and 6 back yokes, among the total 8, have been assembled into the sleeve.

Photo 1(b) shows the armature assembly with 18

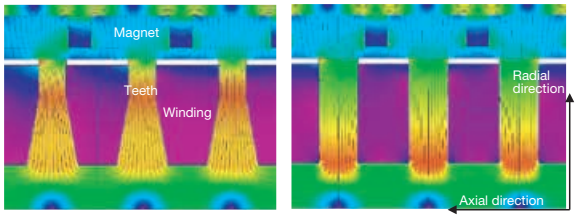

(a) Trapezoid teeth (b) Rectangular teeth

Fig. 6 Flux density of armature

(a) Stator/magnet (being assembled) (b) Armature

Photo 1 Motor assembly

(exactly 24, because of 2 windings per slot) windings installed in the armature core and with 3 green wear rings: two on the both sides of the armature and one at the midpoint.

4 Calculation Model

To determine the theoretical performance of the tertiary prototype, the following sections derive a magnetic field analysis model and a dynamic operation model.

4.1 Magnetic Field Analysis Model

Fig. 7 shows the profile of a magnetic field analysis model used to calculate the stall characteristics and also shows the winding connection.

The model consists of a stator/magnet and an armature and is symmetric with respect to a two-dimensional axis. The sleeve and middle piston use non-magnetic metal.

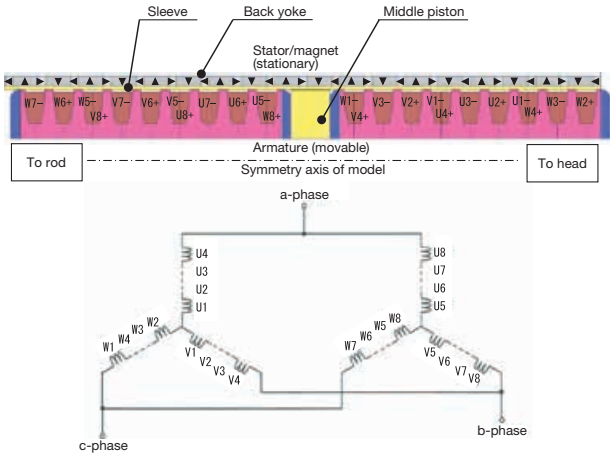

Fig. 7 Magnetic field analysis model

The magnet characteristics values are those at a temperature of 22.9˚C and no eddy current loss in the armature core is not considered.

The winding connection is a parallel configuration of a core assembly on the rod side and another on the head side. The current control has been provided with phase lead compensator of 30° to suppress the magnetic saturation in the armature core.

4.2 Dynamic Operation Model

A dynamic operation model is used to calculate the force-velocity and damping characteristics. Fig. 8 shows the controller, the inverter and the motor. Table 3 shows physical constants used for the calculation. The q-axis flux linkage Φ_q decreases as the current increases, approximating the effect of the magnetic saturation in the armature core.

Table 3 Physical constants

F_c	Current compensator corner frequency
F_{mr}	Frictional force
K_{id}	d-axis control gain
K_{iq}	q-axis control gain
L_d	d-axis inductance
L_q	q-axis inductance
M_ℓ	Inertial mass
R_m	Phase resistance
$R_{\theta 2x}$	Stroke/Angle conversion factor
V_{dc}	Supply voltage of invertor
V_{pw}	PWM voltage
V_{rd}	d-axis command
η_m	Inverter efficiency
Φ_q	q-axis flux linkage

Input to the dynamic operation model is the current command i_m* and output from the model is the stroke x_m and the force f_ℓ. The equation of motion related to the mass M_ℓ can be expressed by Equation (2):

$$M_\ell \ddot{x}_m + F_{mr}\,\mathrm{sgn}\,(\dot{x}_m) = f_\ell - f_c \tag{2}$$

Where, the force f_ℓ is given by Equation (3):

$$f_\ell = \frac{\Phi_q}{R_{\theta 2x}} i_q \tag{3}$$

The motor voltage equation for d-/q-axis models is expressed by Equation (4):

$$\begin{bmatrix} v_d \\ v_q \end{bmatrix} = R_m \begin{bmatrix} i_d \\ i_q \end{bmatrix} + \begin{bmatrix} L_d & 0 \\ 0 & L_q \end{bmatrix} \begin{bmatrix} \dot{i}_d \\ \dot{i}_q \end{bmatrix} + \dot{\theta} \begin{bmatrix} 0 & -L_q \\ L_d & 0 \end{bmatrix} \begin{bmatrix} i_d \\ i_q \end{bmatrix} + \dot{\theta}\Phi_q \begin{bmatrix} 0 \\ 1 \end{bmatrix} \tag{4}$$

Where,

$$i_m = \frac{i_q}{\sqrt{3}} \tag{5}$$

$$\begin{bmatrix} i_d \\ i_q \end{bmatrix} = \sqrt{\frac{2}{3}} \begin{bmatrix} \cos\theta & \cos\left(\theta - \frac{2}{3}\pi\right) & \cos\left(\theta - \frac{4}{3}\pi\right) \\ -\sin\theta & -\sin\left(\theta - \frac{2}{3}\pi\right) & -\sin\left(\theta - \frac{4}{3}\pi\right) \end{bmatrix} \begin{bmatrix} i_a \\ i_b \\ i_c \end{bmatrix} \tag{6}$$

$$\begin{bmatrix} v_a \\ v_b \\ v_c \end{bmatrix} = \sqrt{\frac{2}{3}} \begin{bmatrix} \cos\theta & -\sin\theta \\ \cos\left(\theta - \frac{2}{3}\pi\right) & -\sin\left(\theta - \frac{2}{3}\pi\right) \\ \cos\left(\theta - \frac{4}{3}\pi\right) & -\sin\left(\theta - \frac{4}{3}\pi\right) \end{bmatrix} \begin{bmatrix} v_d \\ v_q \end{bmatrix} \tag{7}$$

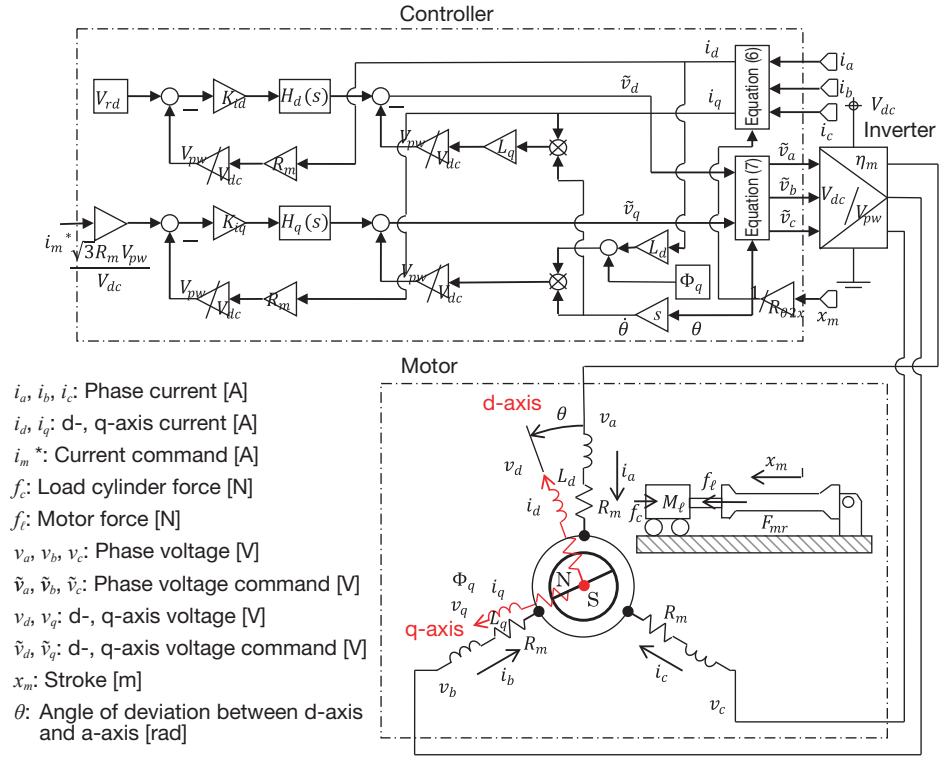

Fig. 8 Dynamic operation model

The PWM operation of the inverter can be approximated by Equation (8):

$$\begin{bmatrix} v_a \\ v_b \\ v_c \end{bmatrix} = \eta_m \frac{V_{dc}}{V_{pw}} \begin{bmatrix} \tilde{v}_a \\ \tilde{v}_b \\ \tilde{v}_c \end{bmatrix} \tag{8}$$

The current compensator for the d-axis can be expressed by Equation (9):

$$\tilde{v}_d = K_{id} H_d(s) \left(V_{rd} - R_m \frac{V_{pw}}{V_{dc}} i_d \right) - \frac{V_{pw}}{V_{dc}} \dot{\theta} L_q i_q \tag{9}$$

Where,

$$H_d(s) = \frac{\dfrac{s}{R_m} + 1}{\dfrac{L_d}{R_m}} \frac{\dfrac{R_m}{L_d}}{\dfrac{s}{2\pi F_c} + 1} \tag{10}$$

The current compensator for the q-axis can be expressed by Equation (11):

$$\tilde{v}_q = K_{iq} H_q(s) \left(\tilde{v}_q^* - R_m \frac{V_{pw}}{V_{dc}} i_d \right) + \frac{V_{pw}}{V_{dc}} \dot{\theta} (\Phi_q + L_d i_d) \tag{11}$$

Where,

$$H_q(s) = \frac{\dfrac{s}{R_m} + 1}{\dfrac{L_q}{R_m}} \frac{\dfrac{R_m}{L_q}}{\dfrac{s}{2\pi F_c} + 1} \tag{12}$$

$$\tilde{v}_q^* = \frac{\sqrt{3} R_m V_{pw}}{V_{dc}} i_m^* \tag{13}$$

Equations (2) through (13) are physical equations expressing the dynamic operation model. For calculation of the damping characteristics, Equation (4) uses $v_d = 0$ and $v_q = 0$ since the a-, b- and c-phase terminals are short-circuited in Fig. 7.

5 Verification Test

5.1 Test Setup

Fig. 9 shows a test setup to evaluate the performance of the tertiary prototype. Table 4 shows the major test equipment. Photo 2 shows how the verification test is carried out.

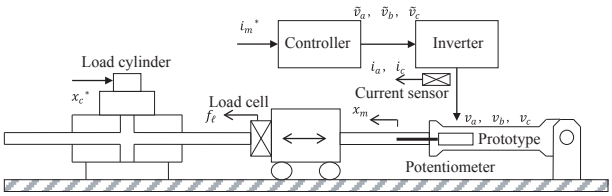

Fig. 9 Test setup

Table 4 Test equipment

	Manufacturer	Model, specifications
Inverter	Myway Plus	MWINV-5022B AC146Arms
Controller	MIS	SEAGALL mini C66 DSP 1.2GHz×4
Load cylinder	Kayaba System Machinery	HTM10-200-07G 10kN, 400mm/s

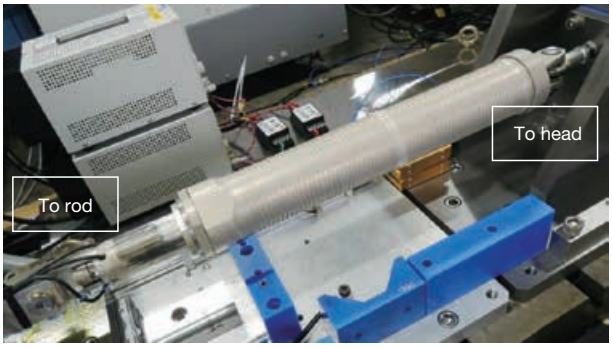

Photo 2 Verification test

A hydraulic load cylinder is located in a position opposite to the prototype and is driven by the stroke control system according to the stroke command x_c*. The load cylinder is equipped with a load cell on the tip to measure the force f_ℓ of the prototype.

The prototype is driven with current control according to the current command i_m via a controller and an inverter. The phase currents i_a and i_c are measured by a current sensor and the phase current i_b is calculated by Equation (14).

$$i_b = - i_a - i_c \tag{14}$$

The stroke x_m of the prototype is measured by the internal potentiometer.

5.2 Low-Speed Operation with Triangular Wave

To verify the sliding property of the armature with the sleeve structure shown in Fig. 4, a low-speed operation test with a triangular wave is conducted. Fig. 10 shows the

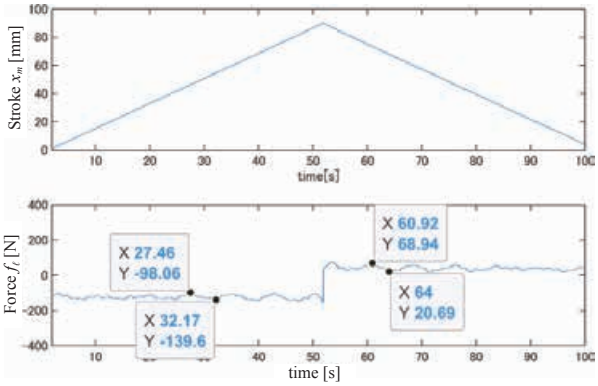

Fig. 10 Low-speed operation with a triangular wave

response, specifically stroke x_m and force f_ℓ, of the prototype when it is forcefully operated by load cylinder with a triangular wave at a frequency of 0.01 Hz and an amplitude of +/-45 mm with the a-, b- and c-phase terminals shown in Fig. 7 left open.

In Fig. 10, the force curve f_ℓ vibrates representing cogging and the rising of the force curve f_ℓ at the turning point of the stroke (about 50 sec.) reflects friction.

Cogging is 41.54 Np-p when the prototype extends or 48.25 Np-p when it retracts, and the normalized cogging with the maximum force described later (in 5.5) is as small as 0.88% to 1.02%. This cogging reduction has been achieved with the 16p18s structure shown in Table 2 and the side piece shown in Fig. 4(b).

The difference between the force during prototype extension and the force during prototype retraction can be used to determine that the frictional force is 163.645 Np-p. Similarly, it can be normalized with the maximum force to be 3.45%, which is not more than the hydraulic actuator friction characteristics (generally 5% to 10%).

It can be determined from the low-speed operation test with a triangular wave (Fig. 10) that the armature with the sleeve structure shown in Fig. 4 has good sliding property.

5.3 Shaking Operation with Sine Wave

To verify that the d-axis current compensator of Equation (9) and the q-axis current compensator of Equation (11) are appropriate, shaking operation with a sine wave is conducted. Using the test setup shown in Fig. 9 with the load cylinder removed from the prototype, the prototype is shaked by the stroke control system using a sine wave at a frequency of 2 Hz and an amplitude of +/-30 mm. The results are shown in Fig. 11.

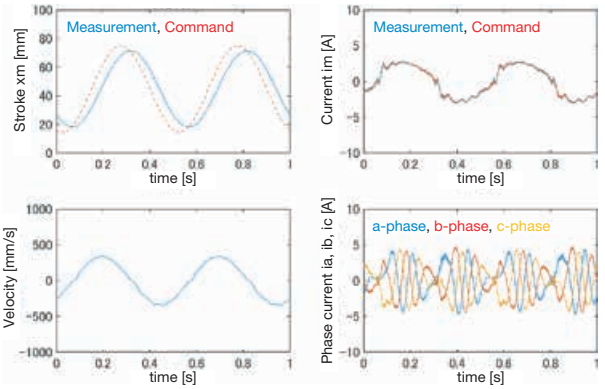

Fig. 11 Shaking operation with a sine wave

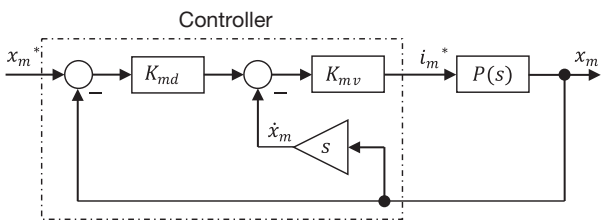

Fig. 12 Stroke control system

Table 5 Constants for stroke control system

K_{md}	Stroke control gain
K_{mv}	Speed control gain

The stroke control system is as shown in Fig. 12 and Table 5. In Fig. 12, $P(s)$ represents the transfer function characteristics from the current command i_m* to the stroke x_m of the dynamic operation model shown in Fig. 8. The stroke control system also has the speed control function as a minor loop. The stroke control frequency has been set to 250 Hz and the speed control frequency to 1 kHz. The current control frequency is 5 kHz and the inverter carrier frequency is 20 kHz in Fig. 8.

According to Fig. 11, the measured value for the current i_m closely follows the command value with no deviation and the phase currents i_a, i_b and i_c do not vibrate, proving that the current control system is stable. Note that the vibration of the current i_m represents a response attributable to cogging.

Based on the shaking operation with a sine wave (Fig. 11), the d-axis current compensator of Equation (9) and the q-axis current compensator of Equation (11) are appropriate.

5.4 Stall Characteristics

The stall characteristics are shown in Fig. 13. The stall characteristics represent the relationship between the current command i_m* and the force f_ℓ when the prototype stroke is retained with the load cylinder and the current command i_m* is given a constant value. Both measured and calculated values for the force f_ℓ represent the average fluctuation in the magnetic pole pitch.

The maximum stall force is 5,034 N @73A during prototype extension and -5,179 N @-73A during prototype retraction, both of which mostly match the calculation results. The non-linearity in the regions of $|i_m^*| > 40$A may be attributable to the magnetic saturation in the armature core.

5.5 Force-Velocity Characteristics

Hydraulic actuators for flight control systems are subjected to a verification test to determine the performance

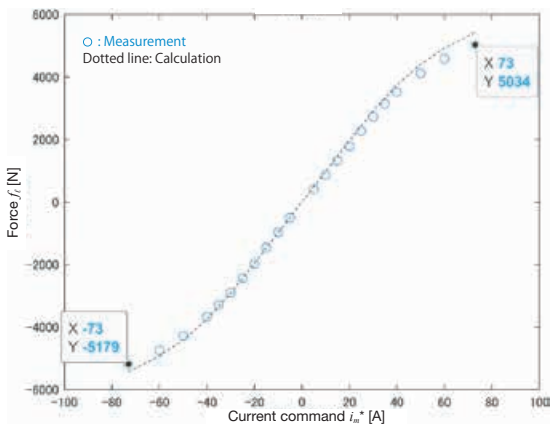

Fig. 13 Stall characteristics

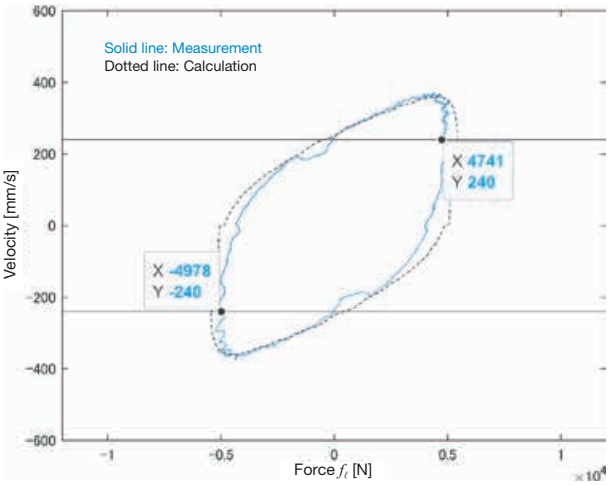

Fig. 14 Force-velocity characteristics

by horizontally applying several hundreds of kilograms of inertia load. Since the application of several hundreds of kilograms of inertia load is dangerous, the load cylinder shown in Fig. 9 is used instead.

The force-velocity characteristics are as shown in Fig. 14. The application conditions can be expressed by Equation (15) and are equivalent to the horizontal application of an inertia load of approx. 200 kg.

$$\left.\begin{aligned} x_c^* &= X_1 \sin(2\pi F_1 t) \\ i_m^* &= I_1 \sin\left(2\pi F_1 t + \tau_1 \frac{\pi}{180}\right) \end{aligned}\right\} \quad (15)$$

Where, X_1 = 30 mm, F_1 = 2 Hz, I_1 = 73 A, τ_1 = -55 deg.

In Fig. 14, Quadrants I and III indicate meter-in operation (power running for electrified operation) and Quadrants II and IV indicate meter-out operation (regenerative). The prototype has the same meter-in and meter-out operation characteristics as those of hydraulic actuators.

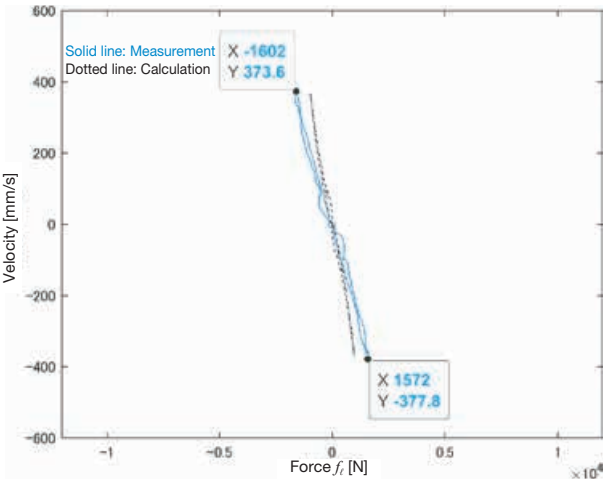

Fig. 15 Damping characteristics

The maximum force is 4,741 N @240 mm/s for prototype extension and -4,978 N @-240 mm/s for prototype retraction. The difference between measurements and calculation may be mainly attributable to the eddy current loss in the armature core.

5.6 Damping Characteristics

The authors assume that the requirements for the electric mechanical actuator to replace the hydraulic equipment relate to the force density as well as the damper operation in case of system shut down. Fig. 15 shows the damping characteristics of the prototype when it is forcefully operated by load cylinder with a sine wave at a frequency of 2 Hz and an amplitude of +/-30 mm with the terminals of the phases a, b and c shown in Fig. 7 left short-circuited.

With a damping factor of 4,224 N/(m/s), the figure indicates linear damping characteristics with small hysteresis. The difference between measurements and calculation may be mainly attributable to the eddy current loss in the armature core as in the force-velocity characteristics. Installing a resistor between the terminals will tune the damping factor to 4,224 N/(m/s) or less, thereby allowing the prototype to be able to serve as a passive damper with a given damping factor in case of system shutdown.

5.7 Force Density

From the maximum force of 4,741 N in 5.5 and the mass of 9.49 kg in Table 2, the force density can be determined to be 499.6 N/kg (= 4,741 N/9.49 kg). The prototypes force density records and the actual data of hydraulic actuators are plotted in Fig. 16. The figure implies that the feasibility of replacing the hydraulic equipment with the electric mechanical actuator has risen.

6 Conclusion

The authors have prototyped the electric mechanical actuator that can be replaced with the hydraulic equipment and carried out a verification test to obtain the following:

(1) The maximum force of 4,741 N @240 mm/s has been achieved through the larger airgap area with the motor structure with the outer stator and inner armature as well as the Halbach arrangement of magnets and the trapezoidal teeth armature.

(2) It has been verified that the prototype shows the friction characteristics not more than those of the hydraulic actuator and the armature has good sliding property thanks to the sleeve structure in which the inner force between the stator and armature is almost zero.

(3) The force density is 499.6 N/kg, which is still below the target level (600 N/kg), but the prototype's force density records and the actual data of the hydraulic actuator's imply that the feasibility for the electric mechanical actuator to replace the hydraulic equipment has risen.

We would like to deeply thank associate professor KANO Yoshiaki of Department of Electrical and Electronic Engineering, Daido University, who designed the motor magnetic circuit for this prototype.

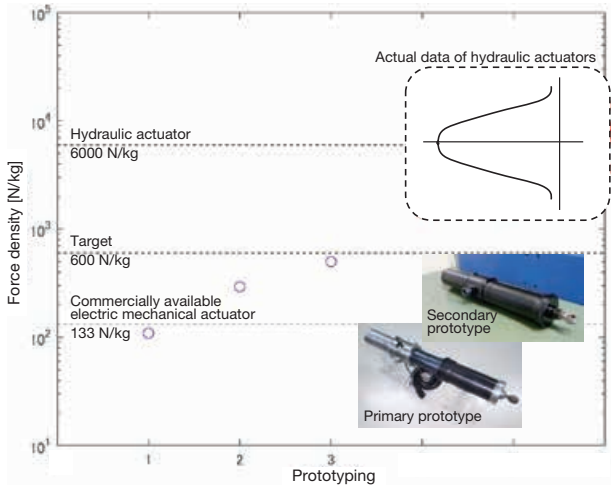

Fig. 16 Force density record

References

1) Michel Todeschi: Airbus-EMAs for flight controls actuation system 2012 status and perspectives, Recent Advances in Aerospace Actuation Systems and Components, Proceedings, (June 13-14 2012).
2) David Blanding: SUBSYSTEM DESIGN AND INTEGRATION FOR THE MORE ELECTRIC AIRCRAFT, Collection of Technical Papers, 5th International Energy Conversion Engineering Conference Vol. 2, (2007).
3) Amine Fraj, Marc Budinger, Toufic El Halabi, Jean-Charles Mare: Modelling approaches for the simulation-based preliminary design and optimization of electromechanical and hydraulic actuation systems, 53rd AIAA/ASME/ASCE/AHS/ASC Structures, Structural Dynamics and Materials Conference, (April 23-26 2012).
4) Yoshiaki Kano, Kousuke Satou: Design and Experimental Verification of a High Force Density Tubular Permanent Magnet Linear Motor for Aerospace Application, AEROTECH EUROPE, (September 24-26 2019).
5) Sato: Development of an Electric Mechanical Actuator for Aircraft with a Cylindrical Linear Motor, KYB Technical Review No.50 (April 2015)

Author

SATO Kosuke

Joined the company in 1984.
Information Technology R&D Sect., Basic Technology R&D Center, Engineering Div.
Engaged in design and development of aircraft equipment.

SHIBAHARA Daichi

Joined the company in 2015.
Information Technology R&D Sect., Basic Technology R&D Center, Engineering Div.
Master's degree in engineering.
Engaged in research and development of elements necessary for electrification of hydraulics

HAKAMADA Shinichiro

Joined the company in 1988.
Chief Researcher, Information Technology R&D Sect., Basic Technology R&D Center, Engineering Div.
Engaged in design and development of various electronic equipment.